# Vigorous lateral export of the meltwater outflow from beneath an Antarctic ice shelf

**Alberto C. Naveira Garabato[1], Alexander Forryan[1], Pierre Dutrieux[2,3], Liam Brannigan[4], Louise C. Biddle[5], Karen J. Heywood[5], Adrian Jenkins[2], Yvonne L. Firing[6] and Satoshi Kimura[2]**

**Affiliations**

[1]Ocean and Earth Science, University of Southampton, National Oceanography Centre, Southampton, SO14 3ZH, UK.

[2]British Antarctic Survey, Cambridge, CB3 0ET, UK.

[3]Lamont-Doherty Earth Observatory of Columbia University, Palisades, NY 10964, USA.

[4]Department of Meteorology, Stockholm University, Stockholm, SE-106 91, Sweden

[5]Centre for Ocean and Atmospheric Sciences, School of Environmental Sciences, University of East Anglia, Norwich, NR4 7TJ, UK.

[6]National Oceanography Centre, Southampton, SO14 3ZH, UK.

***Corresponding author: acng@noc.soton.ac.uk**

**Instability and accelerated melting of the Antarctic Ice Sheet are one of the foremost elements of contemporary global climate change[1,2]. Increased freshwater output from Antarctica is regularly highlighted as a significant player in determining sea level rise[1,3], the fate of Antarctic sea ice and its effect on the Earth's albedo[4,5], on-going changes in global deep-ocean ventilation[3,6], and the evolution of Southern Ocean ecosystems and carbon cycling[7,8]. A key uncertainty in assessing and predicting the impacts of Antarctic ice sheet melting concerns the vertical distribution of the exported meltwater. This is commonly represented by climate-scale models[3-5,9] as a near-surface freshwater input to the ocean, yet measurements around Antarctica reveal the meltwater to be concentrated at deeper levels[10-14]. Here, we use observations of the turbulent**

**properties of the meltwater outflows from beneath a rapidly-melting Antarctic ice shelf to identify the mechanism responsible for the meltwater's deep focus. We show that the initial ascent of the meltwater outflow from the ice shelf cavity triggers centrifugal instability, an overturning instability that grows by extracting kinetic energy from the lateral shear of the background oceanic flow. The instability promotes vigorous lateral export, rapid dilution by turbulent mixing, and the ultimate settling of meltwater at depth. The relevance of this mechanism to a broad spectrum of Antarctic ice shelves is substantiated with an idealised ocean circulation model. Our findings demonstrate that the widely documented presence of meltwater at depth is a dynamically robust feature of Antarctic melting, and call for the representation of its underpinning mechanism in climate-scale models.**

The ice shelves of West Antarctica are losing mass at accelerated rates[2,15], possibly heralding the instability and future collapse of a significant sector of the Antarctic Ice Sheet[16]. The recent rapid thinning of the ice shelves is generally attributed to basal melt driven by warm sub-surface waters originating in the mid-latitude Southern Ocean[17,18], and the mechanisms responsible for the enhanced oceanic delivery of heat to the ice shelves are beginning to be understood[19,20]. In contrast, comparatively little is known about the pathways and fate of the increasing amounts of meltwater pouring into the ocean from the ice shelves. While a widespread freshening of the polar seas fringing Antarctica has been documented over the period of elevated ice shelf mass loss[3,21], the processes regulating the export of meltwater from the ice shelves remain undetermined, with a key focus of debate being the vertical distribution of the exported meltwater[22]. Ice shelf melting is characterised as a surface freshwater source by many climate-scale models[3-5,9], yet this representation appears at odds with the common observation of meltwater being concentrated in the thermocline (at depths of

several hundred metres) across the Antarctic polar seas[10-14].

To resolve this conundrum, we conducted a set of detailed measurements of the hydrographic, velocity and shear microstructure properties of the flow in the close vicinity of the calving front of Pine Island Ice Shelf (PIIS; Fig. 1), one of the fastest-melting ice shelves in Antarctica[15,17]. The observations were obtained in 12 – 15 February 2014 from the *RRS James Clark Ross* under the auspices of the U.K.'s Ice Sheet Stability programme (iSTAR), and were embedded within a cyclonic gyre circulation spanning Pine Island Bay (Fig. 1). This gyre conveys relatively warm Circumpolar Deep Water toward the ice shelf cavity in its northern limb, and exports meltwater-rich glacially-modified water (GMW) away from the cavity in its southern limb[10,23]. Our measurements included sections of 140 hydrographic and 70 microstructure profiles with respective horizontal spacings of ~0.3 km and ~0.6 km, directed either parallel to the entire PIIS calving front at a horizontal distance of 0.5 – 1 km (transects S1A – S1B, Fig.1) or perpendicular to the calving front along the main GMW outflow from the cavity (transect S2, Fig. 1). Further details of the data set are given in the Methods. As regional tidal flows are weak, aliasing of tidal variability by our observations is insignificant to our analysis (see Methods).

An overview of the observed circulation across the PIIS calving front is provided by Fig. 2. Circumpolar Deep Water warmer than 0°C enters the ice shelf cavity beneath the thermocline, centred at a depth of 400 – 500 m (Fig. 2a). Colder Winter Water occupies the upper ocean, and acquires its near-freezing temperature from the strong oceanic heat loss to the atmosphere that occurs in Pine Island Bay throughout much of the year[24]. The layer of Winter Water is punctuated by a series of warmer (>-0.8°C), 1 – 3 km-wide lenses in the 200 – 400 m depth range that are associated with rapid flow

out of the cavity (Fig. 2b) and contain meltwater-rich GMW (Fig. 2c). GMW is warmer than the surrounding Winter Water because it has properties intermediate between the Circumpolar Deep Water and meltwater from which it derives[10]. Although GMW outflows the cavity at several locations, its export is focussed on a fast, narrow jet at the southwestern end of the PIIS calving front, where cross-front speed surpasses 0.5 m $s^{-1}$. Outflowing lenses of GMW are consistently characterised by very intense small-scale turbulence, with rates of turbulent kinetic energy dissipation ($\varepsilon \sim 10^{-7}$ W $kg^{-1}$) and diapycnal mixing ($\kappa \sim 10^{-2}$ $m^2$ $s^{-1}$) exceeding oceanic background values by typically three orders of magnitude (Figs. 2c,d; see Methods). This vigorous turbulent mixing promotes the rapid dilution and dispersal of GMW, and opposes the ascent of the exported meltwater to the upper ocean as a coherent flow.

The cause of the strong turbulence affecting the GMW outflows is unveiled by the observations along transect S2 (Fig. 3), directed normal to the PIIS calving front and approximately following the main GMW export pathway (Fig. 1). The warm signature of GMW extends laterally within the 200 – 400 m depth range and up to ~2 km away from the calving front, contained within a density class (27.7 – 27.8 kg $m^{-3}$) that is stretched vertically relative to offshore conditions (Fig. 3a). This main lens of GMW is connected to a thin filamentary feature with a vertical scale of a few tens of metres that penetrates to ~4 km off the calving front, and that is surrounded by layers of Winter Water. The suggested pattern of three-layered overturning flow is quantitatively endorsed by the measured horizontal and vertical components of velocity (Figs. 3b-c). These show GMW flowing northwestward (i.e. offshore) at ~0.3 m $s^{-1}$ and upward at ~0.01 m $s^{-1}$, consistent with the predominantly lateral circulation and vertical stretching inferred from hydrographic properties. The layers of Winter

Water are seen to flow slowly southeastward (i.e. onshore) and downward at rates of ~0.01 m $s^{-1}$, indicating a role in replenishing the areas near the calving front from which GMW is exported. The GMW's edges are characterised by large horizontal shear (Fig. 3b), abrupt reversals in the direction of vertical motion (Fig. 3c), and greatly elevated rates of turbulent dissipation (Fig. 3d). This suggests that the primarily lateral flow and intense turbulent mixing experienced by GMW, which determine the meltwater's ultimate settling at depth after leaving the ice shelf cavity, are underpinned by the same ocean dynamics.

To elucidate these dynamics, the susceptibility of the circulation to overturning instabilities in the region of the main GMW export pathway is assessed by examining the distribution of potential vorticity ($q$) along transect S2 (Fig. 3e). The procedures for this and subsequent calculations are described in the Methods. A variety of overturning instabilities may develop in a geophysical fluid when $q$ takes the opposite sign to the planetary vorticity[25,26], which is negative in the Southern Hemisphere. These instabilities induce an overturning circulation that extracts energy from the background flow and expends it in the production of small-scale turbulence, mixing the fluid toward a state of marginal stability. The bulk of the transect is characterised by negative values of $q$ on the order of $-1 \times 10^{-9}$ $s^{-3}$, indicative of stable conditions. However, substantial patches of positive $q$ approaching or exceeding $1 \times 10^{-9}$ $s^{-3}$ are also present, notably along the upper and offshore edges of the main lens of GMW and near the terminus of the thin GMW filament. The fulfilment of the instability criterion in these areas suggests that the overturning circulation (Figs. 3b-c) and intense turbulence (Fig. 3d) revealed by our measurements arise from instability of the GMW flow exiting the PIIS cavity.

Overturning instabilities are respectively termed gravitational, symmetric or centrifugal if the fluid's vertical stratification, horizontal stratification or relative vorticity is responsible for meeting the instability criterion, in which case instabilities extract energy from the available potential energy, vertical shear or lateral shear of the background flow[26,27]. The nature of the instability experienced by the GMW outflow is evaluated in two ways. First, the relative importance of the three above factors contributing to the instability criterion is quantified via a balanced Richardson angle analysis[27] of the transect S2 data (see Methods). This indicates that the GMW outflow is primarily subject to centrifugal instability (Fig. 3e, contours), triggered by the large anticyclonic relative vorticity that characterises the outflow (see Methods). Symmetric instability also affects the offshore edge of the main lens of GMW, where significant horizontal stratification occurs as a result of the lens' vertical stretching (Fig. 3a). Second, the energy sources of the three instability types are estimated from the same data set (see Methods), and the extent to which they balance the observed turbulent dissipation is assessed by comparison with the vertical integral of ε (Fig. 3f). The measured overturning circulation is found to principally extract energy from the lateral shear of the background flow, as expected from centrifugal instability, and to do so at rates of 0.1 – 0.5 W $m^{-2}$ that are broadly consistent with those of turbulent dissipation. Energy sources linked to gravitational and symmetric instabilities are generally negligible. Note that a close spatio-temporal correspondence between the energy source of centrifugal instability and turbulent dissipation is not expected, as centrifugal instability takes several hours to grow and generate the secondary instabilities that directly induce turbulent dissipation (see Methods).

In conclusion, our observations of the turbulent properties of the meltwater outflows from beneath the fast-melting PIIS show that centrifugal instability is a key

contributor to the vigorous mixing that is responsible for the concentration of meltwater at the thermocline commonly documented across and beyond Pine Island Bay[10-13]. The mechanism is triggered by the injection of high-buoyancy, meltwater-rich GMW at the PIIS calving front (Fig. 4). As GMW is more buoyant than the water above, it initially rises toward the upper ocean while undergoing gravitational instability, mixing and entraining ambient waters. This mixing and entrainment induce a localised vertical stretching and tilting of a density class slightly shallower than the ice shelf's base. The horizontal pressure gradient associated with the tilted density surfaces drives a geostrophic flow along the calving front that develops large anticyclonic relative vorticity in excess of the local planetary vorticity, and thus becomes unstable to centrifugal instability. This instability promotes an overturning circulation that transports GMW laterally away from the calving front and dilutes it rapidly through intense turbulent mixing, thereby arresting the meltwater's initial buoyant ascent.

This mechanism is reproduced by an idealised ocean circulation model configured with parameters and forcings appropriate to the PIIS outflow (see Methods). The model suggests that our observations provide a representative characterisation of the mechanism's dynamics, despite the measurements' omission, for reasons of navigational safety, of the initial gravitational instability adjacent to the base of the calving front. The model further indicates that the mechanism is likely to be of widespread relevance to buoyant meltwater outflows from beneath other Antarctic ice shelves, many of which are characterised by more modest melting rates[2,14]. Our findings thus show that the widely observed focussing of meltwater at depth is a dynamically robust feature of Antarctic ice sheet melting, and suggest that representation of the effects of centrifugal instability is critical to the realism of

climate-scale ocean models with melting ice sheets. As explicit resolution of the mechanism (with respective horizontal and vertical scales of ~100 m and ~10 m; see Methods) is presently beyond the capability of even regional models of ice shelf – ocean interaction[24,28], the development of a parameterisation of centrifugal instability of meltwater outflows from beneath floating ice shelves is called for.

## Methods

**PIIS calving front data set.** A set of targeted measurements of the hydrographic, velocity and shear microstructure properties of the ocean adjacent to the Pine Island Ice Shelf (PIIS) calving front was collected during expedition JR294/295 of the *RRS James Clark Ross* between 12 and 15 February 2014, supported by the *Ocean2ice* project of the U.K.'s Ice Sheet Stability programme (iSTAR, http://www.istar.ac.uk; see Fig. 1). The measurements were organised in three transects: two (transects S1A and S1B) directed parallel to and jointly spanning the PIIS calving front at a distance of 0.5 – 1 km from the front; and the other (transect S2) directed normally to the calving front along the main glacially-modified water (GMW) outflow from the cavity at a distance of 0.5 – 4.5 km from the front. During each transect, a lightly-tethered, free-falling Rockland Scientific International VMP-2000 microstructure profiler was deployed continuously behind the slowly moving (at ~0.5 m $s^{-1}$) ship to acquire vertical profiles of measurements between approximately 10 m beneath the ocean surface and 100 m above the ocean floor. Temperature, salinity and pressure were measured on both down- and upcasts, whereas shear microstructure was solely recorded on downcasts, thereby yielding a reduced number of profiles and coarser inter-profile separation for microstructure measurements (70 profiles ~0.6 km apart, vs. 140 profiles ~0.3 km apart for hydrographic observations). Horizontal and vertical velocity measurements over the uppermost 600 m of the water column were obtained

with a shipboard 75 kHz RD Instruments acoustic Doppler current profiler. The slow motion of the ship through the water and exceptionally calm sea state permitted the detection of significant vertical water velocities along transect S2 (Fig. 3c). Full details of the data set acquisition may be found in the JR294/95 cruise report, available online at https://www.bodc.ac.uk/data/information_and_inventories/cruise_inventory/report/jr294.pdf .

**Calculation of turbulent dissipation and mixing rates from microstructure measurements.** The rate of dissipation of turbulent kinetic energy, ε, was computed from microstructure measurements as $\varepsilon = 7.5\nu\overline{(\partial u'/\partial z)^2}$, where ν is the molecular viscosity and $\overline{(\partial u'/\partial z)^2}$ is the variance in the vertical shear of the horizontal velocity over the resolved turbulent wavenumber range[29]. Shear variance was calculated every 0.5 m, using shear spectra computed over a bin width of 1 s and integrated between 1 Hz and the spectral minimum in the 10 – 25 Hz band (or the 25 – 100 Hz band for $\varepsilon > 10^{-7}$ W kg$^{-1}$). The sampling rate of the vertical microstructure profiler was 512 Hz. The rate of turbulent diapycnal mixing, κ, was estimated from ε as $\kappa = \Gamma\,\varepsilon / N^2$, where Γ is a mixing efficiency (taken as 0.2 as pertinent to shear-driven turbulence) and $N$ is the buoyancy frequency[30].

**Tides near the PIIS calving front.** The set of hydrographic, velocity and microstructure measurements discussed in this article was obtained in three sampling periods (corresponding to the three transects in Fig. 1) of 8 – 35 hours between 12 and 15 February 2014. As these periods are comparable to or exceed the primary time scales of oceanic tidal variability, our observations may potentially be contaminated by aliased tidal flows. To dispel this concern, we hereby examine the amplitude of

tidal variability near the PIIS calving front.

Circum-Antarctic tidal models indicate that tidal forcing is modest in the Amundsen Sea Embayment in general, and in the area adjacent to and beneath the PIIS in particular[31,32], with characteristic tidal currents of O(1 cm $s^{-1}$). As these are substantially smaller than the O(10 cm $s^{-1}$) horizontal flows that we measure in association with meltwater outflows (Figs. 2b and 3b), the models suggest that tides are of secondary importance in forcing exchanges between the PIIS cavity and the open ocean offshore.

To corroborate this model prediction, we consider a 2-year-long (January 2012 – January 2014) time series of horizontal velocity obtained with a mooring deployed in the area of the main meltwater outflow from the PIIS (at a distance of ~8 km from the calving front, see Fig. 1) under the auspices of the iSTAR programme. The mooring was instrumented with a current meter and an upward-looking acoustic Doppler current profiler (ADCP) with a range of ~160 m, deployed at respective depths of 671 m and 380 m. An analysis of the tides measured by both of these instruments was conducted using the T_tide software package[33]. The diagnosed tidal currents are shown in Fig. S1, alongside the local mean flows. Monthly-mean sub-inertial flows vary between 2 and 15 cm $s^{-1}$, and the average flow over the 2-year record is 7.5 cm $s^{-1}$ for the ADCP and 5.3 cm $s^{-1}$ for the current meter. In contrast, tidal currents are typically one order of magnitude smaller, and rarely exceed 1 cm $s^{-1}$. This disparity between sub-inertial and tidal flows is confirmed by spectral and wavelet analyses of the mooring data (not shown), which indicate that the bulk of the kinetic energy resides in sub-inertial frequencies. Although tidal and near-inertial flows may be amplified within a few hundred metres of the PIIS calving front[34], sub-inertial flows

intensify even more notably (to velocities in excess of 30 cm $s^{-1}$, ref. 23). Thus, significant contamination of our measurements by tidal flows is highly unlikely.

**Calculation of meltwater concentration.** Meltwater concentration is estimated from temperature and salinity for each measured hydrographic profile, using the method in ref. (35). The method assumes that each measured water parcel derives its properties from the mixing of three source water masses: Circumpolar Deep Water and Winter Water (indicated in Fig. S2), and glacial meltwater. This assumption breaks down in the upper part of the water column (specifically, above the core of the Winter Water at a depth of ~200 m), where atmospheric forcing influences the ocean's temperature and salinity. The assumption's failure results in a bias of meltwater concentration estimates in the upper ocean toward high values[35]. In spite of this bias, enhanced meltwater concentrations in excess of 8‰ are apparent in the 200 – 400 m depth range (Figs. 2c-d) in areas where the flow is directed out of the PIIS cavity (Fig. 2b), and concentration characteristically decreases toward the surface in the uppermost 100 m of the water column.

This vertical distribution is representative of other hydrography-based estimates of meltwater concentration in the vicinity of the Amundsen Sea ice shelves[10], which occasionally indicate the presence of enhanced concentrations near the surface. In contrast, noble gas-based estimates, which do not suffer from a near-surface high bias, regularly show a clearer focussing of meltwater in the thermocline[11,14].

**Intensification of turbulent kinetic energy dissipation in meltwater outflows.** The enhancement of the rate of dissipation of turbulent kinetic energy (ε) in meltwater outflows from the PIIS cavity (Fig. 2) is succinctly illustrated by an examination of

the ε measurements along transects S1A – S1B, which span the entire PIIS calving front, in potential temperature – salinity space (Fig. S2). The mixing line between the warm, saline Circumpolar Deep Water and the cold, fresh Winter Water is consistently characterised by background levels of turbulent dissipation ($\varepsilon \sim 10^{-10}$ W kg$^{-1}$). In contrast, waters that are warmer than this mixing line at each salinity, which contain meltwater-rich GMW, regularly exhibit significantly elevated values of ε. The most intense turbulent dissipation ($\varepsilon \sim 10^{-7}$ W kg$^{-1}$) affects the waters with the highest meltwater content, i.e. those that deviate the most from the Circumpolar Deep Water – Winter Water mixing line.

**Calculation of potential vorticity.** The Ertel potential vorticity, $q$, is defined as $q = (f\hat{k} + \nabla\times\boldsymbol{u}) \cdot \nabla b$, where $f$ is the Coriolis parameter, $\hat{k}$ is the vertical unit vector, **u** is the three-dimensional velocity vector, and $b$=-$g\rho/\rho_0$ is the buoyancy ($g$ is the acceleration due to gravity, $\rho$ is density, and $\rho_0$ is a reference density)[25]. To calculate $q$ along transect S2 (Fig. 3e), we adopted the approximation $q \approx (f + \partial v/\partial x)N^2 - f|\partial \boldsymbol{u_h}/\partial z|^2$, where $\boldsymbol{u_h} = (u, v)$ is the horizontal velocity vector referenced to the along-transect ($u$) and across-transect ($v$) directions, $x$ and $y$ respectively refer to the along-transect and across-transect distances, and $N$ is the buoyancy frequency. This approximation is associated with two possible sources of error. First, the vertical component of relative vorticity, $\zeta = \partial v/\partial x - \partial u/\partial y$, is approximated by its first term, i.e. $\zeta \approx \partial v/\partial x$. This is likely to induce an underestimation of the magnitude of $\zeta$ of up to a factor of 2, particularly as the flow approaches solid body rotation for large values of $\zeta$ (ref. 36). In spite of this bias, $\zeta$ regularly exceeds $f$ by a factor of 1-3 in areas of the transect where $q$ is positive (Fig. S3). Our diagnostics of overturning instabilities may thus be viewed as quantitatively conservative, and qualitatively robust to this source of error. Second, the flow is assumed to be in geostrophic

balance to leading order. This assumption is supported by the close agreement between the transect-mean geostrophic shear and measured vertical shear in $v$ along transect S2 (Fig. S4, right panel). Structure in the measured vertical shear on horizontal scales of O(1 km) is largely consistent with geostrophic balance too, as evidenced by the close alignment of flow reversals in $v$ with changes in the sign of isopycnal slopes (Fig. S4, left panel).

**Characterisation of overturning instabilities and their associated energy sources.** Overturning instabilities develop in areas where $fq < 0$ (refs. 25, 26). This criterion may be equivalently expressed as $\phi_{Ri_B} < \phi_c$ (ref. 26), where the balanced Richardson number angle $\phi_{Ri_B} = \tan^{-1}(-N^{-2}|\partial \boldsymbol{u_h}/\partial z|^2)$ and the critical angle $\phi_c = \tan^{-1}\left(-1 - f^{-1}\nabla\times\boldsymbol{u}\cdot\hat{k}\right) \approx \tan^{-1}(-1 - f^{-1}(\partial v/\partial x))$. The same assumptions as in the calculation of $q$ were adopted. When the instability criterion is met, the nature of the instability may be determined from the value of $\phi_{Ri_B}$ (ref. 27; Fig. 3e). Gravitational instability is associated with $-180° < \phi_{Ri_B} < -135°$ and $N^2 < 0$. Gravitational – symmetric instability corresponds to $-135° < \phi_{Ri_B} < -90°$ and $N^2 < 0$. Symmetric instability is indicated by $-90° < \phi_{Ri_B} < -45°$, with $N^2 > 0$ and $f^{-1}\nabla\times\boldsymbol{u}\cdot\hat{k} > 0$. Symmetric – centrifugal instability is implied by $-90° < \phi_{Ri_B} < -45°$, with $N^2 > 0$ and $f^{-1}\nabla\times\boldsymbol{u}\cdot\hat{k} < 0$. Centrifugal instability is linked to $\phi_{Ri_B} > -45°$, with $N^2 > 0$ and $f^{-1}\nabla\times\boldsymbol{u}\cdot\hat{k} < 0$.

Overturning instabilities derive their kinetic energy from a combination of convective available potential energy (gravitational instability), vertical shear production (symmetric instability) and lateral shear production (centrifugal instability)[27]. The rate of extraction of available potential energy along the S2 transect was estimated from

measurements of the vertical velocity ($w$) and buoyancy as $F_b = \overline{w'b'}$, where the overline denotes a spatial average over the area of the instability and primes the deviation from that average. Here, the spatial average was computed horizontally at each depth level along the entire transect, to capture the buoyancy flux induced by the significant up- and downwelling flows associated with the instability (Fig. 3c). The rates of vertical and lateral shear production were estimated from velocity measurements as $P_{vrt} = -\overline{\boldsymbol{u_h}'w'} \cdot (\partial\overline{\boldsymbol{u_h}}/\partial z)$ and $P_{lat} = -\overline{\boldsymbol{u_h}'v_s'} \cdot (\partial\overline{\boldsymbol{u_h}}/\partial s)$, respectively, where $s$ is the horizontal coordinate perpendicular to the depth-integrated flow and $v_s$ is the component of $\boldsymbol{u_h}$ in that direction. Here, the spatial average was calculated vertically at each horizontal location over the maximum common depth of the transect, to determine the momentum fluxes associated with the three-layered overturning flow (Fig. 3b).

**Idealised model of the meltwater outflow from beneath an Antarctic ice shelf.** An idealised model of the meltwater outflow from beneath an Antarctic ice shelf is constructed to corroborate our interpretation of the measurements near the PIIS calving front, gain further insight into the dynamics of the outflow, and explore the relevance of our results to buoyant meltwater outflows from beneath other ice shelves.

Simulations are carried out using the MITgcm[37] in non-hydrostatic mode. The model set-up is a two-dimensional domain in the y-z plane analogous to a transect perpendicular to an ice shelf calving front (i.e. similar to transect S2 in Fig. 3). The set-up permits a circulation in the along-domain direction that can support an across-domain geostrophic flow. The domain is bounded by vertical walls at y = 0 km and y = 5.76 km, with the latter wall taken to be the location of the calving front. The domain is 300 m deep, broadly similar to the measured draft at the PIIS calving front.

Horizontal and vertical grid spacings are 4 m and 3 m, respectively.

Simulations are run on the U.K. ARCHER supercomputer, a Cray XC30 system. The time-stepping interval is 1 s. The Coriolis parameter is set to $f = -1.4 \times 10^{-4}$ s $^{-1}$. A linear equation of state is employed with a thermal expansion coefficient $\alpha = 2 \times 10^{-4}$ $K^{-1}$. Laplacian operators are used for vertical viscosity and tracer diffusion, with viscous / diffusive coefficients of $4 \times 10^{-5}$ $m^{-2}$ $s^{-1}$. Biharmonic operators are used for horizontal viscosity and tracer diffusion. The horizontal viscous Smagorinsky coefficient is 3, and the constant horizontal diffusive coefficients are $1 \times 10^{-1}$ $m^{-4}$ $s^{-1}$. A 7$^{th}$-order monotonicity-preserving tracer advection scheme is used for temperature and the passive tracer[38]. The MITgcm's default centred 2$^{nd}$-order scheme is used to advect momentum. A non-dimensional bottom drag of $3 \times 10^{-3}$ is applied to dissipate kinetic energy.

The initial condition is of no flow anywhere in the domain. The initial temperature profile has uniform stable stratification everywhere, with the exception of the buoyant restoring region at the bottom-right of the domain, as described below. The magnitude of the initial buoyancy frequency of $7.7 \times 10^{-3}$ $s^{-1}$ corresponds to the average value observed near the PIIS calving front along transect S2. The continuous inflow of buoyant water from beneath the ice shelf is represented by restoring the initial temperature at the bottom right, as indicated in Fig. S5. In our primary, PIIS-based experiment (labelled 'Main'), the temperature anomaly (defined with respect to temperature away from the right-hand wall) increases linearly from 0 to 1 K at the base of the wall over a distance of 160 m. This temperature anomaly is equivalent to a buoyancy anomaly of $2 \times 10^{-3}$ m $s^{-2}$, and is chosen to approximately match the difference between the buoyancy of GMW and that of Winter Water measured along

transects S1A – S1B. To allow a steady state to be reached, the initial temperature profile on the left-hand side of the domain is also restored over a distance of 200 m from the edge of the domain. The restoring time scale is 10 seconds for both restoring regions. A passive tracer *A* with an initial concentration of 1 is released in the restoring region at the base of the right-hand wall. This passive tracer is intended as a proxy for meltwater in the observations. The initial concentration of the passive tracer is also restored at the base of the right-hand wall. No buoyancy or frictional fluxes are applied at the surface.

When the Main experiment begins, an overturning flow develops on the lower right-hand side of the domain (Fig. S6a). This motion is initially due to the positive buoyancy anomaly in the restoring region, which gives rise to lateral pressure gradients not balanced by a geostrophic velocity. While the unbalanced lateral pressure gradients initially occur only at the very bottom of the domain, the unstable stratification induces a fast-growing gravitational instability with a growth time scale of approximately 2 minutes. The gravitational instability leads to columns of buoyant fluid of ~30 m width being accelerated vertically through the lower half of the domain next to the right-hand wall. These columns of buoyant fluid result in unbalanced lateral pressure gradients in the area of the buoyancy anomaly throughout the lower half of the domain in the opening hours of the simulation (Fig. S6a). In response to these unbalanced lateral pressure gradients, overturning occurs through the lower half of the domain (Fig. S6a). The associated geostrophic adjustment causes the fluid that was convected to 150 m depth to be accelerated to the left, i.e. away from the area of the initial buoyancy perturbation. This along-domain flow is then deflected to the left by the Coriolis force. As the along-domain velocity is zero at the right-hand wall and negative in the interior of the domain, the along-domain flow is divergent and leads to

vortex stretching and anticyclonic relative vorticity (Fig. S6c).

Considering potential vorticity is most useful in interpreting the development of the unstable flow in the Main experiment[25-27]. The area of the initial buoyancy anomaly exhibits positive potential vorticity due to its unstable stratification at the outset of the simulation. Two hours after the start of the simulation (Fig. S6e), this fluid still has positive potential vorticity despite some vertical mixing with stably stratified waters during the convective stage. The overturning motion then increases the stratification of the fluid and maintains its positive potential vorticity by the generation of the aforementioned anticyclonic relative vorticity (Fig. S6c). After approximately 1 day (or 2 inertial periods), isopycnals dome around the level of neutral buoyancy (Fig. S6b), and a cross-domain geostrophic jet forms around the nose of the adjusted region near (3.6 km, 160 m). This jet has large anticyclonic lateral shear. Although remnants of unstable stratification contribute in a small fraction of the area, the prominent anticyclonic relative vorticity associated with the jet (Fig. S6d) is principally responsible for the positive potential vorticity in the adjustment region of domed isopycnals (Fig. S6f). This leads to the development of centrifugal instability, which is apparent in the cross-domain velocity as bands of alternating flow, for example in the 100 – 240 m depth range between x = 4 km and x = 5.3 km (Fig. S6f). The weak vertical stratification and pronounced vertical shear in this area induce Kelvin-Helmholtz instabilities that mix the potential vorticity anomalies back toward stability. Overall, restoring of the buoyancy anomaly at the base of the right-hand wall provides a persistent input of destabilizing positive potential vorticity into the adjustment region that is balanced by the input of stabilizing negative potential vorticity across the potential vorticity gradient around the adjustment region. Equivalently, restoring of the buoyancy anomaly at the right-hand boundary provides

a continual input of available potential energy that is balanced by the loss of kinetic energy in the jet to centrifugal instability.

Despite its highly idealised nature, the Main experiment reproduces all the key features of the meltwater outflow from beneath the PIIS apparent in our observations at a distance greater than 500 m from the calving front: a layered horizontal flow structure associated with large anticyclonic relative vorticity ($\zeta / f < -1$) and positive potential vorticity, conducive to centrifugal instability and a predominantly lateral export of the meltwater (tracer) at depth. The simulation further suggests that our measurements fail to sample the gravitational instability experienced by the outflow as it leaves the cavity. This convection underpins the localised vertical stretching that initiates the centrifugal instability.

Further experiments (labelled 'Perturbation') where the temperature anomaly is decreased to 0.5 K (i.e. half of that in the Main simulation, and equivalent to a buoyancy anomaly of $\sim 1 \times 10^{-3}$ m s$^{-2}$) or increased to 1.5 K (i.e. 1.5 times larger than that in the Main simulation, and equivalent to a buoyancy anomaly of $\sim 3 \times 10^{-3}$ m s$^{-2}$) are also performed to illustrate the robustness of the mechanism diagnosed in the simulation above to a range of forcings. Glaciological and oceanographic observations around Antarctica suggest that, while the rates of melting of Antarctic ice shelves vary by up to one order of magnitude[39] (with the PIIS lying near the upper end of the range), the buoyancy contrast between the waters entering and outflowing ice shelf cavities varies comparatively less across very different melting conditions, being typically of O($10^{-3}$ m s$^{-2}$) (e.g., compare the stratification observed near the PIIS calving front with that measured near the Filchner – Ronne ice shelf[13], which is characterised by a melting rate one order of magnitude smaller). We thus vary the

initial temperature of the idealised meltwater outflow in the model to yield sizeable buoyancy anomaly perturbations within the general range suggested by observations. A more exhaustive investigation considering the influence of offshore stratification and other factors (e.g., three-dimensional processes) on the behaviour and dynamics of meltwater outflows will be conducted as a follow up to this study.

The Perturbation experiments produce very similar results to the Main experiment in that isopycnals are domed and a centrifugally unstable jet is formed next to the buoyancy source (Fig. S7). The depth of the nose of the adjusted region becomes shallower as the buoyancy anomaly is increased, in a manner consistent with the shoaling of the depth of neutral buoyancy. The horizontal extent of the adjusted region becomes larger as the buoyancy anomaly is enhanced, as expected from the increase of the Rossby deformation radius that results from the larger vertical extent and greater buoyancy contrast of the adjusted region. The time scale of adjustment also becomes shorter as the buoyancy anomaly increases (not shown). This is in line with the theoretical prediction of the growth time scale of centrifugal instability[26], given by $(f\,(f + \zeta))^{-1/2}$, which decreases from ~2 h in the 0.5 K simulation to ~1 h in the 1.5 K simulation as the anticyclonic relative vorticity of the adjusted region increases from ~2|f| to ~5|f|.

A final set of two experiments (labelled 'Rotation') is conducted to clarify the relative roles of gravitational and centrifugal instabilities (which, as noted in the preceding discussion, occur concurrently in the Main and Perturbation experiments) in determining the vertical distribution of the buoyant water. In these simulations, the magnitude of the Coriolis parameter is gradually reduced from its value in the Main experiment ($f = -1.4 \times 10^{-4}$ s$^{-1}$) to a value one order of magnitude smaller ($f = -1 \times 10^{-5}$

$s^{-1}$) and ultimately to zero. Since the occurrence of symmetric and centrifugal instabilities is suppressed in the limit of vanishing rotation, reducing $f$ is an effective way to differentiate the respective impacts of gravitational and centrifugal instabilities on the buoyant water's fate. The key non-dimensional parameter that measures the relative importance of buoyancy and rotation in each simulation is $N/f$ (ref. 40), which takes a value of 18 in the Main experiment, 254 in the weak rotation experiment, and infinity in the non-rotating experiment. All other numerical parameters and boundary conditions in the Rotation experiments are identical to those in the Main experiment.

The vertical distribution of the passive tracer tracking the buoyant water is significantly influenced by rotation, and hence the occurrence or absence of centrifugal instability (Fig. S8a). One day after injection, the tracer distribution is more tightly concentrated around a narrow depth range and centred at a shallower depth in the Rotation experiments with a small or zero Coriolis parameter than in the Main experiment. Examination of the tracer distribution as a function of temperature (Fig. S8b) shows more modest differences between the three simulations, indicating that most of the deepening and broadening of the vertical tracer profile with increasing rotation seen in Fig. S8a is related to changes in the depths of isopycnal surfaces. However, the presence of an appreciable deepening (i.e. translation toward colder temperatures) and broadening of the tracer peak with increasing rotation in Fig. S8b suggests that intensified turbulent diapycnal mixing also plays a significant role in determining the vertical dispersal of the tracer. Thus, the occurrence of centrifugal instability as rotation increases from zero toward realistic values significantly deepens and broadens the vertical distribution of the buoyant water, both by adjusting the vertical horizons of isopycnal surfaces and by elevating turbulent diapycnal mixing. These effects of rotation in our two-dimensional experiments are consistent with

findings in three-dimensional simulations of buoyant plumes from deep-ocean vents for similar values of *N/f* (ref. 40).

*Overview of model experiments*

The suite of idealised experiments presented above suggests that the mechanism of centrifugal instability and predominantly lateral export of the meltwater outflow from beneath the PIIS documented by our measurements is relevant to a broad spectrum of Antarctic ice shelves, including those characterised by substantially more modest melting rates. Circumstantial evidence of the persistence of the process at the PIIS and its occurrence at other Antarctic ice shelves is available from the few previous high-resolution surveys conducted at the calving fronts of the PIIS[23] and other ice shelves[41-43], which indicate the presence of sharp outflowing jets characterised by a velocity structure, lateral shear and relative vorticity resembling those in our observations. The mechanism documented in this study is distinct from the convective adjustment highlighted by previous modelling investigations of meltwater outflows from beneath Antarctic ice shelves and from Greenland tidewater glaciers (which, unlike our simulations, do not consider the effects of the Earth's rotation[44-46]), and yields a significantly enhanced lateral export and reduced upward penetration of the meltwater. Our results echo the dynamics of dry mesoscale convective systems in the atmosphere[47], in which the combination of convection-induced vertical stretching and geostrophic adjustment leads to the formation of jets that are susceptible to centrifugal instability.

**Code availability.** The model code and scripts used in generating the simulations analysed in this article are available from https://github.com/braaannigan/Vigorous_lateral_export.

**Data availability.** The observational data analysed in this study are available from the British Oceanographic Data Centre at https://www.bodc.ac.uk/data/information_and_inventories/cruise_inventory/report/13405/. Model simulation data are available from L.B. on reasonable request.

## References


1. IPCC *Climate Change 2013: The Physical Science Basis* (eds Stocker, T. F. *et al.*) (Cambridge Univ. Press, 2014); http://www.climatechange2013.org/report/full-report

2. Shepherd, A. *et al.* A reconciled estimate of ice-sheet mass balance. *Science* **338**, 1183-1189 (2012).

3. Rye, C. D. *et al.* Rapid sea-level rise along the Antarctic margins in response to increased glacial discharge. *Nature Geosci.* **7**, 732-735 (2014).

4. Richardson, G., Wadley, M. R., Heywood, K. J., Stevens, D. P. & Banks, H. T. Short-term climate response to a freshwater pulse in the Southern Ocean. *Geophys. Res. Lett.* **32**, doi: 10.1029/2004GL021586 (2005).

5. Bintanja, R., van Oldenborgh, G. H., Drijfhout, S. S., Wouters, B. & Catsman, C. A. Important role for ocean warming and increased ice-shelf melt in Antarctic sea-ice expansion. *Nature Geosci.* **6**, 376-379 (2013).

6. Purkey, S. G. & Johnson, G. C. Global contraction of Antarctic Bottom Water between the 1980s and 2000s. *J. Clim.* **25**, 5830-5844 (2012).

7. Arrigo, K. R., van Dijken, G. L. & Strong, A. L. Environmental controls of marine productivity hot spots around Antarctica. *J. Geophys. Res.* **120**, 5545-5565 (2015).

8. Arrigo, K. R., van Dijken, G. & Long, M. Coastal Southern Ocean: A strong anthropogenic $CO_2$ sink. *Geophys. Res. Lett.* **35**, doi: 10.1029/2008GL035624 (2008).

9. Swart, N. C. & Fyfe, J. C. The influence of recent Antarctic ice sheet retreat on simulated sea ice area trends. *Geophys. Res. Lett.* **40**, doi:10.1002/grl.50820 (2013).

10. Dutrieux, P. *et al.* Strong sensitivity of Pine Island Ice-Shelf melting to climatic variability. *Science* **343**, 174-178 (2014).

11. Hohmann, R., Schlosser, P., Jacobs, S., Ludin, A. & Weppernig, R. Excess helium and neon in the southeast Pacific: tracers for glacial meltwater. *J. Geophys. Res.* **107**, doi:10.1029/2000JC000378 (2002).

12. Loose, B., Schlosser, P., Smethie, W. M. & Jacobs, S. An optimized estimate of

glacial melt from the Ross Ice Shelf using noble gases, stable isotopes, and CFC transient tracers. *J. Geophys. Res.* **114**, doi:10.1029/2008JC005048 (2009).

13. Nicholls, K. W., Østerhus, S., Makinson, K., Gammelsrød, T. & Fahrbach, E. Ice-ocean processes over the continental shelf of the southern Weddell Sea, Antarctica: A review. *Rev. Geophys.* **47**, doi: 10.1029/2007RG000250 (2009).

14. Kim, I. *et al.* The distribution of glacial meltwater in the Amundsen Sea, Antarctica, revealed by dissolved helium and neon. *J. Geophys. Res.*, doi:10.1002/2015JC011211 (2016).

15. Paolo, F. S., Fricker, H. A. & Padman, L. Volume loss from Antarctic ice shelves is accelerating. *Science* **348**, 327-331 (2015).

16. Feldmann, J. & Levermann, A. Collapse of the West Antarctic Ice Sheet after local destabilization of the Amundsen Basin. *Proc. Natl. Aca. Sci.* **112**, 14191-14196 (2015).

17. Pritchard, H. D. *et al.* Antarctic ice-sheet loss driven by basal melting of ice shelves. *Nature* **484**, 502-505 (2012).

18. Joughin, I., Alley, R. B. & Holland, D. M. Ice-sheet response to oceanic forcing. *Science* **338**, 1172-1176 (2012).

19. Thoma, M., Jenkins, A. Holland, D. & Jacobs, S. Modelling Circumpolar Deep Water intrusions on the Amundsen Sea continental shelf, Antarctica. *Geophys. Res. Lett.* **35**, doi:10.1029/2008GL034939 (2008).

20. Stewart, A. L. & Thompson, A. F. Eddy-mediated transport of warm Circumpolar Deep Water across the Antarctic shelf break. *Geophys. Res. Lett.* **42**, 432-440 (2015).

21. Schmidtko, S., Heywood, K. J., Thompson, A. F. & Aoki, S. Multidecadal warming of Antarctic waters. *Science* **346**, 1227-1231 (2014).

22. Pauling, A. G., Bitz, C. M., Smith, I. J. & Langhorne, P. J. The response of the Southern Ocean and Antarctic sea ice to freshwater from ice shelves in an Earth system model. *J. Clim.* **29**, 1655-1672.

23. Thurnherr, A. M., Jacobs, S. S., Dutrieux, P. & Giulivi, C. F. Export and circulation of ice cavity water in Pine Island Bay, West Antarctica. *J. Geophys. Res.* **119**, 1754-1764 (2014).

24. St. Laurent, P., Klinck, J. & Dinniman, M. Impact of local winter cooling on the melt of Pine Island Glacier, Antarctica. *J. Geophys. Res.* **120**, doi:10.1002/2015jc010709 (2015).

25. Hoskins, B. J. The role of potential vorticity in symmetric stability and instability. *Quart. J. Roy. Met. Soc.* **100**, 480-482 (1974).

26. Haine, T. W. N. & Marshall, J. Gravitational, symmetric, and baroclinic instability of the ocean mixed layer. *J. Phys. Oceanogr.* **28**, 634-658 (1998).

27. Thomas, L. N., Taylor, J. R., Ferrari, R. & Joyce, T. M. Symmetric instability in the Gulf Stream. *Deep-Sea Res. II* **91**, 96-110 (2013).

28. Nakayama, Y., Timmermann, R., Rodehacke, C. B., Schröder, M. & Hellmer, H. H. Modeling the spreading of glacial meltwater from the Amundsen and Bellingshausen Seas. *Geophys. Res. Lett.* **41**, doi:10.1002/2014GL061600 (2014).

29. Oakey, N. S. Determination of the rate of dissipation of turbulent energy from simultaneous temperature and velocity shear microstructure measurements. *J. Phys. Oceanogr.* **12**, 256-271 (1982).

30. Osborn, T. R. Estimates of the local rate of vertical diffusion from dissipation measurements. *J. Phys. Oceanogr.* **10**, 83-89 (1980).

31. Padman, L., Fricker, H. A., Coleman, R., Howard, S. & Erofeeva, L. A new tide model for the Antarctic ice shelves and seas. *Ann. Glaciol.* **34,** 247–254 (2002).

32. Robertson, R. Tides, the PIG, and 'warm' water. *IOP Conf. Ser. Earth Environ. Sci.* **11,** 012002 (2010).

33. Pawlowicz, R., Beardsley, B. & Lentz, S. Classical tidal harmonic analysis including error estimates in MATLAB using T_TIDE. *Comput. Geosci.* **28,** 929–937 (2002).

34. Robertson, R. Tidally induced increases in melting of Amundsen Sea Ice Shelves. *J. Geophys. Res. Ocean.* **118,** 1–8 (2013).

35. Jenkins, A. The impact of melting ice on ocean waters. *J. Phys. Oceanogr.* **29**, 2370-2381 (1999).

36. Rudnick, D. L. On the skewness of vorticity in the upper ocean. *Geophys. Res. Lett.* **28**, 2045-2048 (2001).

37. Marshall, J., Adcroft, A., Hill, C., Perelman, L. & Heisey, C. A finite-volume, incompressible Navier – Stokes model for studies of the ocean on parallel computers. *J. Geophys. Res.* **102**, 5753-5766 (1997).

38. Daru, V. & Tenaud, C. High order one-step monotonicity-preserving schemes for

unsteady compressible flow calculations. *J. Comp. Phys.* **193**, 563-594 (2004).

39. Depoorter, M. A., Bamber, J. L., Griggs, J. A., Lenaerts, J. T. M., Ligtenberg, S. R. M., van den Broeke, M. R. & Moholdt, G. Calving fluxes and basal melt rates of Antarctic ice shelves. *Nature* **502**, 89-92 (2013).

40. Fabregat Tomàs, A., Poje, A. C., Özgökmen, T. M. & Dewar, W. K. Effects of rotation on turbulent buoyant plumes in stratified environments. *J. Geophys. Res.* **121**, doi:10.1002/2016JC011737.

41. Randall-Goodwin, E. & thirteen others. Freshwater distributions and water mass structure in the Amundsen Sea Polynya region, Antarctica. *Elem. Sci. Anth.* **3**, doi:10.12952/journal.elementa.000065 (2015).

42. Jenkins, A. & Jacobs, S. Circulation and melting beneath George VI Ice Shelf, Antarctica. *J. Geophys. Res.* **113**, doi:10.1029/2007JC004449 (2008).

43. Herráiz-Borreguero, L., Coleman, R., Allison, I., Rintoul, S. R., Craven, M. & Williams, G. D. Circulation of modified Circumpolar Deep Water and basal melt beneath the Amery Ice Shelf, East Antarctica. *J. Geophys. Res.* **120**, doi: 10.1029/2007JC004449 (2015).

44. Xu, Y., Rignot, E., Menemenlis, D. & Koppes, M. Numerical experiments on subaqueous melting of Greenland tidewater glaciers in response to ocean warming and enhanced subglacial discharge. *Ann. Glaciol.* **53**, 229-234 (2012).

45. Cowton, T., Slater, D., Sole, A., Goldberg, D. & Nienow, P. Modeling the impact of glacial runoff on fjord circulation and submarine melt rate using a new subgrid-scale parameterization for glacial plumes. *J. Geophys. Res.* **120**, 796-812 (2015).

46. Carroll, D., Sutherland, D. A., Shroyer, E. L., Nash, J. D., Catania, G. A. & Steams, L. A. Modelling turbulent subglacial meltwater plumes: Implications for fjord-scale buoyancy-driven circulation. *J. Phys. Oceanogr.* **45**, 2169-2185 (2015).

47. Shutts, G. J. & Gray, M. E. B. A numerical modelling study of the geostrophic

adjustment process following deep convection. *Q. J. R. Meteorol. Soc.* **120**, 1145–1178 (1994).

**Acknowledgements** The iSTAR programme is supported by the Natural Environment Research Council of the U.K. (grant NE/J005703/1). A.C.N.G. acknowledges the support of a Philip Leverhulme Prize, the Royal Society, and the Wolfson Foundation. We are grateful to the scientific party, crew and technicians on the *RRS James Clark Ross* for their hard work during data collection.

**Author Contributions** A.C.N.G. and A.F. designed and conducted the data analysis, with contributions from P.D. and L.C.B. L.B. designed and conducted the idealised model experiments. K.J.H. led the JR294/295 research cruise. All authors contributed to the scientific interpretation of the results.

**Author Information** Reprints and permissions information is available at www.nature.com/reprints. Correspondence and requests for materials should be addressed to acng@noc.soton.ac.uk

## Figure legends

**Figure 1 | Map of the study region.** Positions of hydrographic / microstructure profiles are shown by circles, coloured by the mean meltwater content (ml $l^{-1}$) in the 100 – 700 m depth range estimated as in ref. (10). Horizontal velocity (gridded in 3 km × 3 km bins) in the upper ocean (0 – 300 m) measured with a ship-mounted acoustic Doppler current profiler is indicated by white vectors, with black vectors showing measurements in January 2009 (ref. 23). Seabed elevation (m) is denoted by

blue shading, ice photography (TERRA image from 27 January 27 2014) by grey shading, and ice shelf / ice sheet boundaries by white lines. Transects S1A, S1B and S2 are labelled. The red rectangle marks the position of a mooring used in assessing the significance of tidal flows (see Methods).

**Figure 2 | Transect along the PIIS calving front**. (a) Potential temperature (θ, colour) and neutral density (in kg $m^{-3}$, black contours), with positions of stations indicated by grey tick marks at the base of the figure. (b) Across-transect velocity (*v*), with positive values directed northwestward (out of the PIIS cavity). (c) Rate of turbulent kinetic energy dissipation (ε, a metric of the intensity of small-scale turbulence, in colour), with contours of meltwater concentration (see Methods) superimposed. (d) Rate of diapycnal mixing (κ, colour), with contours as in (c). Both ε and κ are calculated from microstructure measurements (see Methods). Distance is measured from the origin of the S1A transect, at the southwestern corner of the PIIS calving front. The break point near 30 km indicates the transition from the S1A transect to the S1B transect. The characteristic vertical extent of the PIIS is shown by the grey rectangle at the right-hand axis of each panel.

**Figure 3 | Transect along the main outflow from the PIIS calving front.** (a) Potential temperature (θ, colour), neutral density (in kg $m^{-3}$, black contours) and mixed layer depth (determined from the maximum in buoyancy frequency, dashed white contour), with positions of stations indicated by grey tick marks on the upper axis. (b) Along-transect velocity (*u*, colour), with positive values directed southeastward (into the PIIS cavity). (c) Vertical velocity (*w*, colour), with positive values directed upward. Potential temperature contours are shown at intervals of 0.2°C in (b)-(c). (d) Rate of turbulent kinetic energy dissipation (ε, colour), with

contours of meltwater concentration (see Methods) superimposed. (e) Potential vorticity ($q$, colour). Areas of positive $q$ (indicative of overturning instabilities) are outlined. The outline shading denotes the instability type (GRV = gravitational; SYM = symmetric; CTF = centrifugal; see Methods). The characteristic vertical extent of the PIIS is shown by the grey rectangle at the right-hand axis of (a)-(e). (f) Comparison between the vertically integrated (between depths of 50 m, below the base of the upper-ocean mixed layer, and 610 m, the maximum common depth of the transect) rates of turbulent kinetic energy dissipation (ε, yellow bars) and of turbulent kinetic energy production associated with gravitational instability ($F_b$, white line), symmetric instability ($P_{vrt}$, grey line) and centrifugal instability ($P_{lat}$, black line). See Methods.

**Figure 4 | Schematic of the meltwater outflow from beneath the PIIS.** The direction of cross-calving-front flow is indicated by the thick arrows, and the direction of the along-calving-front flow is shown by the circle. The sense of rotation of the flow as it experiences centrifugal instability is indicated in the upper axis (ζ = relative vorticity; f = planetary vorticity). Surfaces of constant density are denoted by solid white contours, and the upper-ocean mixed layer base is marked by the dashed white line. The three distinct water masses are labelled.

**Figure S1 | Tidal flows near the PIIS calving front.** Major axis of tidal ellipse for each individual tidal constituent from a mooring deployed in the area of the main meltwater outflow from the PIIS (Fig. 1), at nominal depths of 310 m (measured with an ADCP, black symbols) and 671 m (measured with a current meter, red symbols). Tidal ellipses are computed using harmonic analysis[33]. The amplitude of each ellipse's major axis is shown by dots, and error estimates are displayed as bars. The 2-

year-record-mean flow speed for each of the two instruments is indicated in the inset.

**Figure S2 | Turbulent dissipation along the PIIS calving front.** Rate of dissipation of turbulent kinetic energy (ε, in colour) along transects S1A – S1B, displayed as a function of potential temperature (θ) and salinity (*S*). The loci of the three distinct water masses in the region are indicated by the labels in italics (CDW = Circumpolar Deep Water; GMW = glacially-modified water; WW = Winter Water).

**Figure S3 | Cross-transect velocity and relative vorticity along the main outflow from the PIIS calving front.** (a) Cross-transect velocity (*v*, colour) along transect S2, with positive values directed northeastward. Potential temperature contours are shown at intervals of 0.2°C (see Fig. 3a). (b) Ratio of relative vorticity ($\zeta$) to planetary vorticity (*f*) along the same transect (colour), where $\zeta \approx \partial v/\partial x$. Areas of positive potential vorticity (indicative of overturning instabilities) are outlined as in Fig. 3e. The outline shading denotes the instability type (GRV = gravitational; SYM = symmetric; CTF = centrifugal; see Methods). The characteristic vertical extent of the PIIS is shown by the grey rectangle at the right-hand axis of each panel.

**Figure S4 | Assessment of geostrophic balance along the main outflow from the PIIS calving front.** (a) Cross-transect velocity (*v*, colour) along transect S2, with positive values directed norththeastward. Neutral density (in kg $m^{-3}$) is indicated by black contours. (b) Profiles of transect-mean cross-transect velocity (*v*) and geostrophic velocity (*gvel*), relative to the depth-averaged velocity.

**Figure S5 | Initial condition in the Main simulation of an idealised meltwater outflow from beneath an Antarctic ice shelf.** The initial temperature distribution is

shown by the colour shading, and the locations of the unstable restoring region (representing the meltwater outflow) and of the stable restoring region (representing ambient offshore conditions) are indicated.

**Figure S6 | Evolution of the idealised meltwater outflow in the Main experiment.** Distributions of the (a) along-domain velocity, (c) relative vorticity normalised by the planetary vorticity, (e) potential vorticity and (g) passive tracer concentration, 2 hours after the start of the simulation. Panels (b), (d), (f) and (h) show the same variables as (a), (c), (e) and (g), respectively, 120 hours after the start of the simulation. Temperature contours are shown at intervals of 0.2°C in all panels. Units are indicated next to the colour bars.

**Figure S7 | Evolution of the idealised meltwater outflow in the Perturbation experiments with reduced and enhanced forcings.** Distributions of the (a) along-domain velocity, (c) relative vorticity normalised by the planetary vorticity, (e) potential vorticity and (g) passive tracer concentration, 120 hours after the start of the reduced forcing (0.5 K) simulation. Panels (b), (d), (f) and (h) show the same variables as (a), (c), (e) and (g), respectively, 120 hours after the start of the enhanced forcing (1.5 K) simulation. Temperature contours are shown at intervals of 0.2°C in all panels. Units are indicated next to the colour bars.

**Figure S8 | Vertical distribution of passive tracer on day 1 for varying planetary rotation.** (a) Horizontally integrated tracer concentration (normalised to a common value) as a function of depth for the Main experiment with realistic rotation ($f = 1.4 \times 10^{-4}$ s$^{-1}$), and for the two Rotation experiments with weak ($f = 1 \times 10^{-5}$ s$^{-1}$) and no ($f = 0$) rotation. (b) Domain-mean tracer concentration (normalised to a common value) in

temperature bins of 0.05 K width. The (a) depth or (b) temperature of neutral buoyancy for the simulated outflow is shown as a horizontal black line.

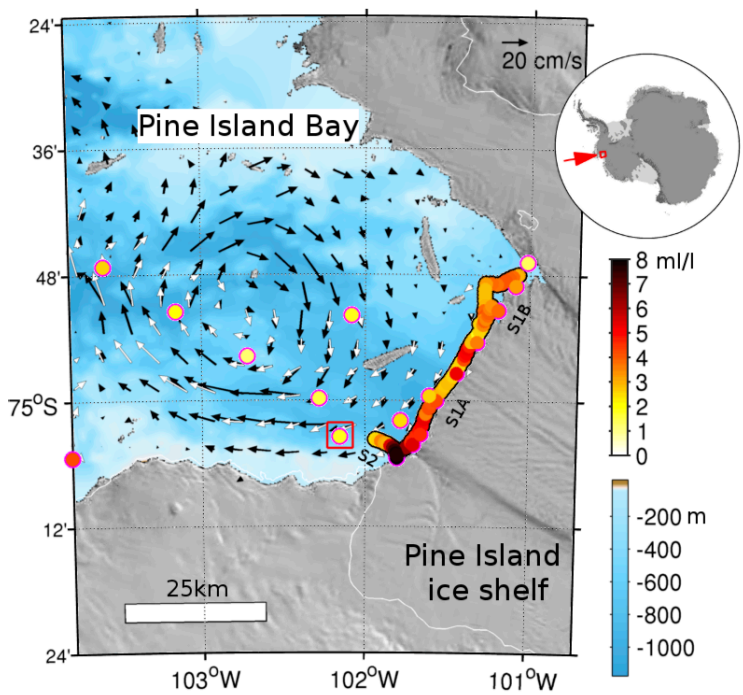


**Figure 1 | Map of the study region.** Positions of hydrographic / microstructure profiles are shown by circles, coloured by the mean meltwater content (ml $l^{-1}$) in the 100 – 700 m depth range estimated as in ref. (10). Horizontal velocity (gridded in 3 km × 3 km bins) in the upper ocean (0 – 300 m) measured with a ship-mounted acoustic Doppler current profiler is indicated by white vectors, with black vectors showing measurements in January 2009 (ref. 23). Seabed elevation (m) is denoted by blue shading, ice photography (TERRA image from 27 January 27 2014) by grey shading, and ice shelf / ice sheet boundaries by white lines. Transects S1A, S1B and S2 are labelled. The red rectangle marks the position of a mooring used in assessing the significance of tidal flows (see Methods).

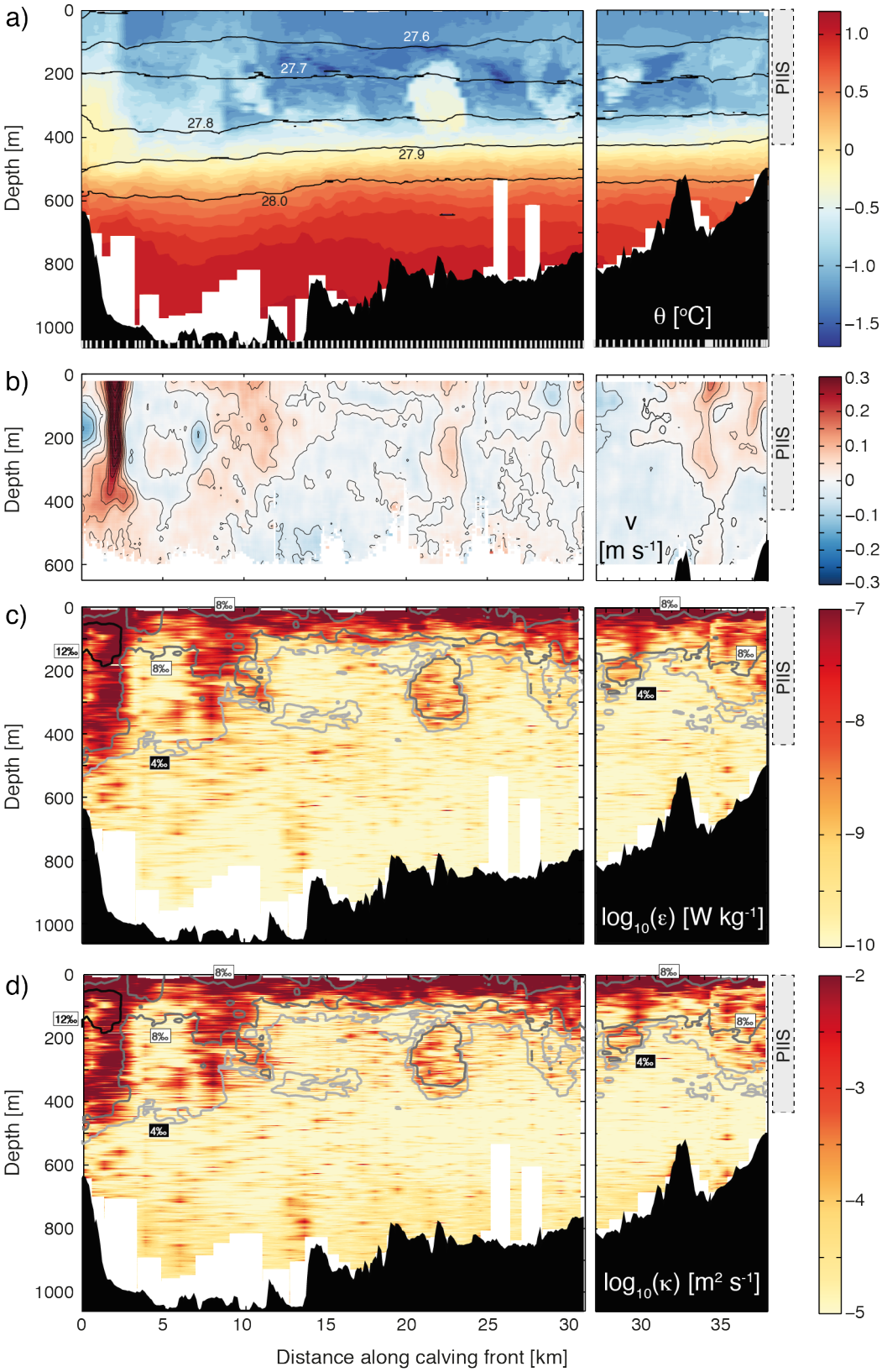


**Figure 2 | Transect along the PIIS calving front**. (a) Potential temperature (θ, colour) and neutral density (in kg m$^{-3}$, black contours), with positions of stations indicated by grey tick marks at the base of the figure. (b) Across-transect velocity ($v$), with positive values directed northwestward (out of the PIIS cavity). (c) Rate of

turbulent kinetic energy dissipation (ε, a metric of the intensity of small-scale turbulence, in colour), with contours of meltwater concentration (see Methods) superimposed. (d) Rate of diapycnal mixing (κ, colour), with contours as in (c). Both ε and κ are calculated from microstructure measurements (see Methods). Distance is measured from the origin of the S1A transect, at the southwestern corner of the PIIS calving front. The break point near 30 km indicates the transition from the S1A transect to the S1B transect. The characteristic vertical extent of the PIIS is shown by the grey rectangle at the right-hand axis of each panel.

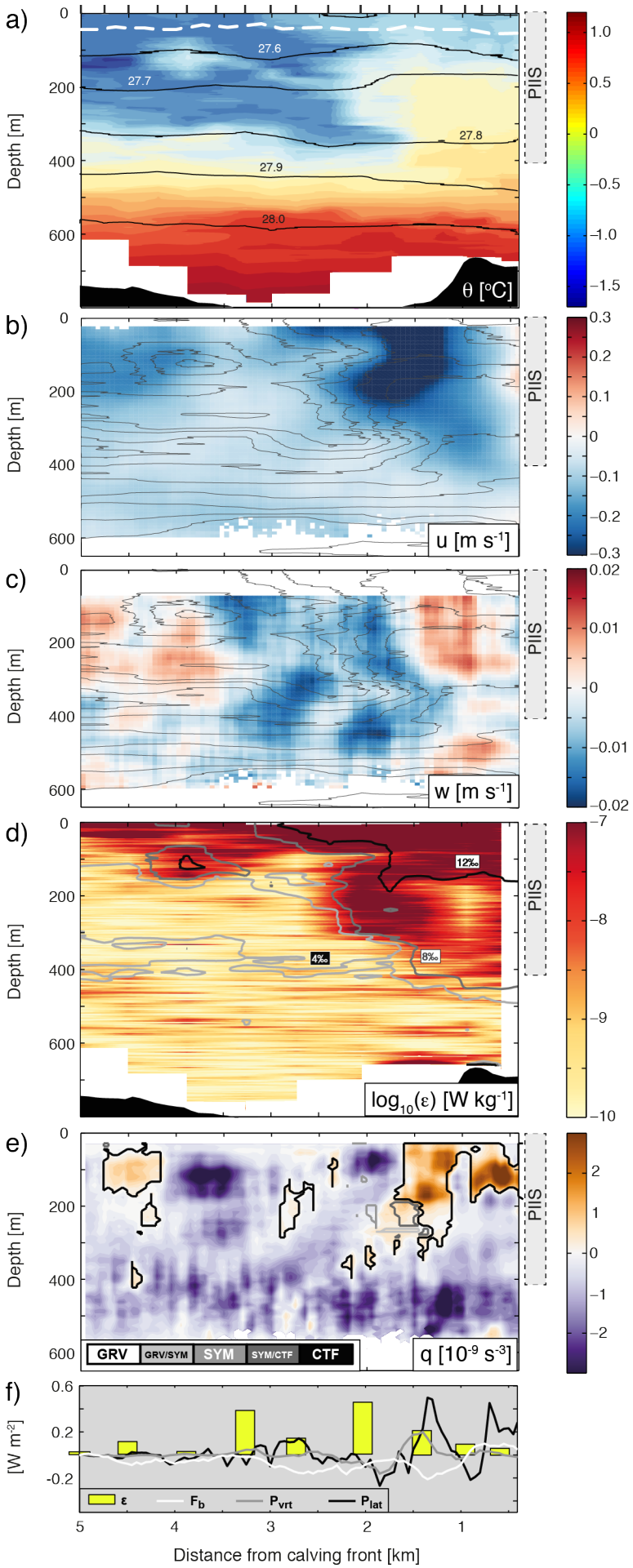
a)
b)
c)
d)
e)
f)
Depth [m]
PIIS
27.6
27.7
27.8
27.9
28.0
θ [°C]
u [m s-1]
w [m s-1]
12‰
4‰
8‰
log10(ε) [W kg-1]
GRV
GRV/SYM
SYM
SYM/CTF
CTF
q [10-9 s-3]
[W m-2]
ε
Fb
Pvrt
Plat
Distance from calving front [km]

**Figure 3 | Transect along the main outflow from the PIIS calving front.** (a) Potential temperature (θ, colour), neutral density (in kg $m^{-3}$, black contours) and mixed layer depth (determined from the maximum in buoyancy frequency, dashed white contour), with positions of stations indicated by grey tick marks on the upper axis. (b) Along-transect velocity ($u$, colour), with positive values directed southeastward (into the PIIS cavity). (c) Vertical velocity ($w$, colour), with positive values directed upward. Potential temperature contours are shown at intervals of 0.2°C in (b)-(c). (d) Rate of turbulent kinetic energy dissipation (ε, colour), with contours of meltwater concentration (see Methods) superimposed. (e) Potential vorticity ($q$, colour). Areas of positive $q$ (indicative of overturning instabilities) are outlined. The outline shading denotes the instability type (GRV = gravitational; SYM = symmetric; CTF = centrifugal; see Methods). The characteristic vertical extent of the PIIS is shown by the grey rectangle at the right-hand axis of (a)-(e). (f) Comparison between the vertically integrated (between depths of 50 m, below the base of the upper-ocean mixed layer, and 610 m, the maximum common depth of the transect) rates of turbulent kinetic energy dissipation (ε, yellow bars) and of turbulent kinetic energy production associated with gravitational instability ($F_b$, white line), symmetric instability ($P_{vrt}$, grey line) and centrifugal instability ($P_{lat}$, black line). See Methods.

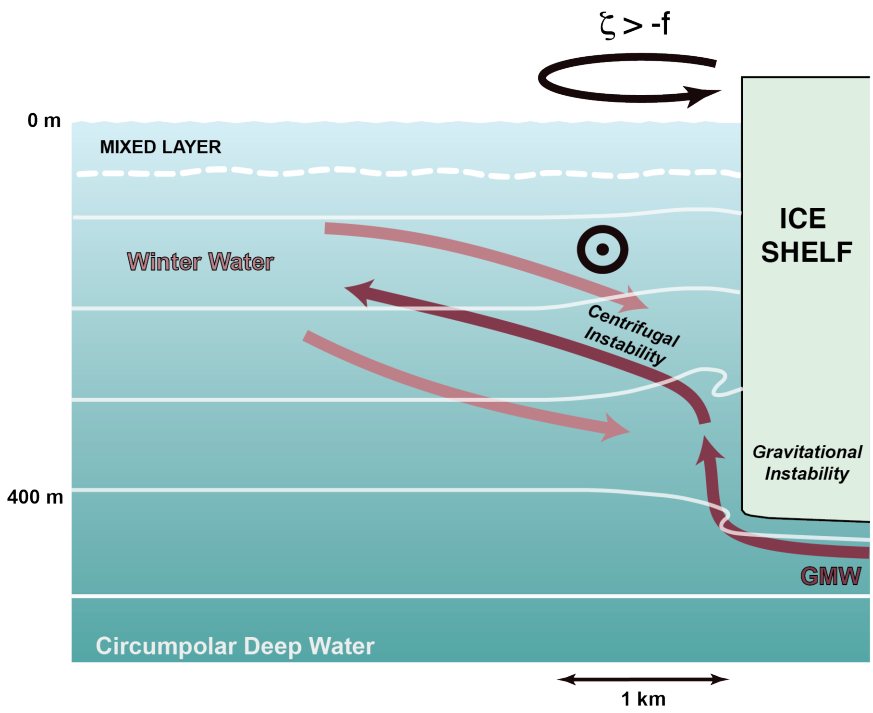


**Figure 4 | Schematic of the meltwater outflow from beneath the PIIS.** The direction of cross-calving-front flow is indicated by the thick arrows, and the direction of the along-calving-front flow is shown by the circle. The sense of rotation of the flow as it experiences centrifugal instability is indicated in the upper axis (ζ = relative vorticity; f = planetary vorticity). Surfaces of constant density are denoted by solid white contours, and the upper-ocean mixed layer base is marked by the dashed white line. The three distinct water masses are labelled.

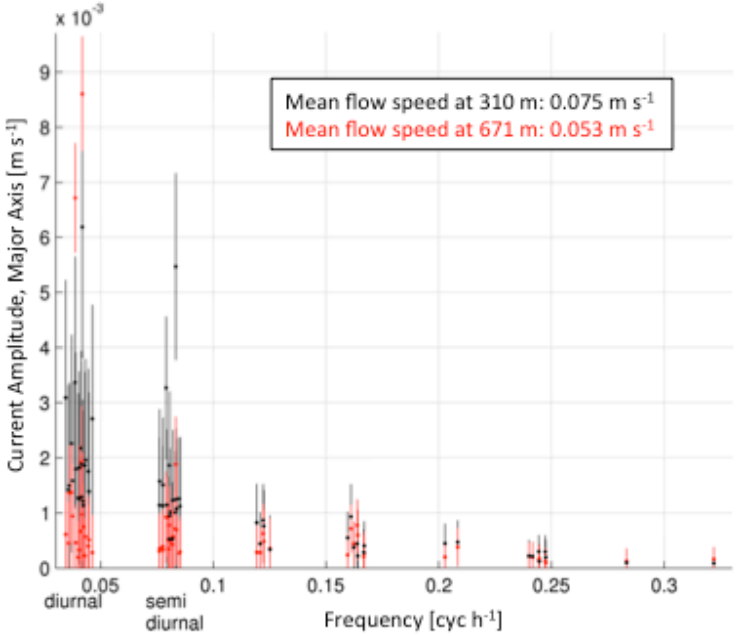


**Figure S1 | Tidal flows near the PIIS calving front.** Major axis of tidal ellipse for each individual tidal constituent from a mooring deployed in the area of the main meltwater outflow from the PIIS (Fig. 1), at nominal depths of 310 m (measured with an ADCP, black symbols) and 671 m (measured with a current meter, red symbols). Tidal ellipses are computed using harmonic analysis[33]. The amplitude of each ellipse's major axis is shown by dots, and error estimates are displayed as bars. The 2-year-record-mean flow speed for each of the two instruments is indicated in the inset.

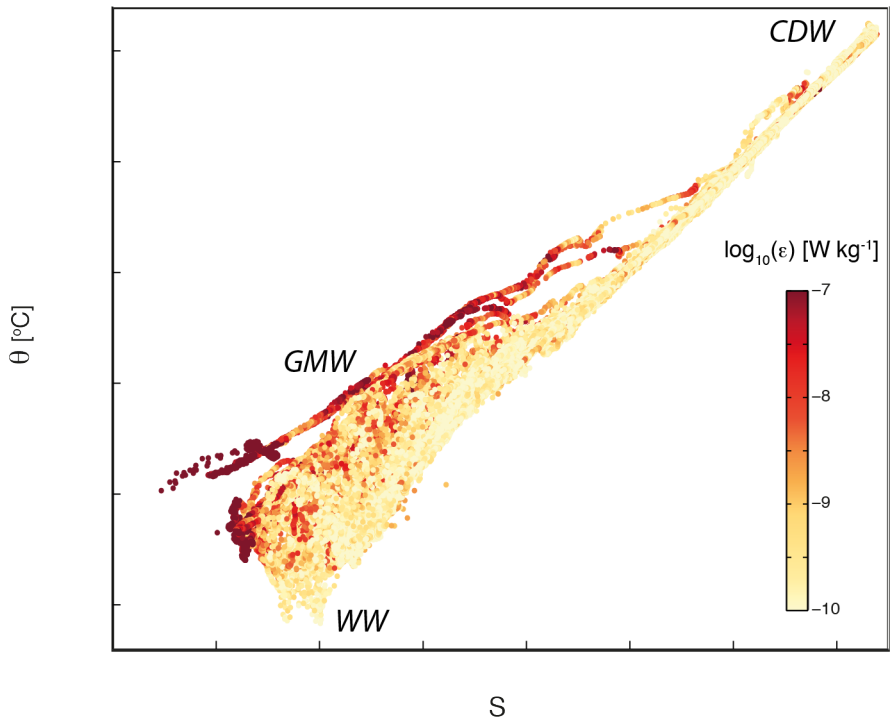


**Figure S2 | Turbulent dissipation along the PIIS calving front.** Rate of dissipation of turbulent kinetic energy (ε, in colour) along transects S1A – S1B, displayed as a function of potential temperature (θ) and salinity (*S*). The loci of the three distinct water masses in the region are indicated by the labels in italics (CDW = Circumpolar Deep Water; GMW = glacially-modified water; WW = Winter Water).

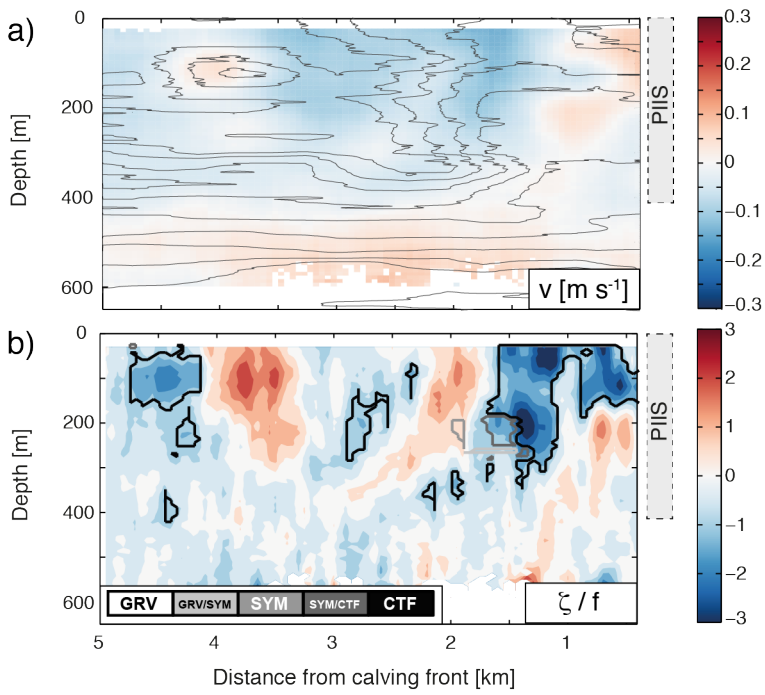


**Figure S3 | Cross-transect velocity and relative vorticity along the main outflow from the PIIS calving front.** (a) Cross-transect velocity ($v$, colour) along transect S2, with positive values directed northeastward. Potential temperature contours are shown at intervals of 0.2°C (see Fig. 3a). (b) Ratio of relative vorticity ($\zeta$) to planetary vorticity ($f$) along the same transect (colour), where $\zeta \approx \partial v/\partial x$. Areas of positive potential vorticity (indicative of overturning instabilities) are outlined as in Fig. 3e. The outline shading denotes the instability type (GRV = gravitational; SYM = symmetric; CTF = centrifugal; see Methods). The characteristic vertical extent of the PIIS is shown by the grey rectangle at the right-hand axis of each panel.

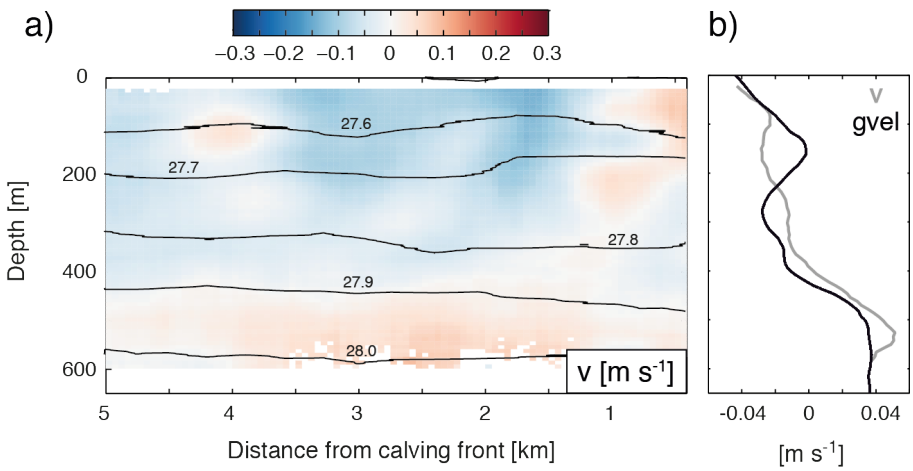


**Figure S4 | Assessment of geostrophic balance along the main outflow from the PIIS calving front.** (a) Cross-transect velocity (*v*, colour) along transect S2, with positive values directed norththeastward. Neutral density (in kg $m^{-3}$) is indicated by black contours. (b) Profiles of transect-mean cross-transect velocity (*v*) and geostrophic velocity (*gvel*), relative to the depth-averaged velocity.

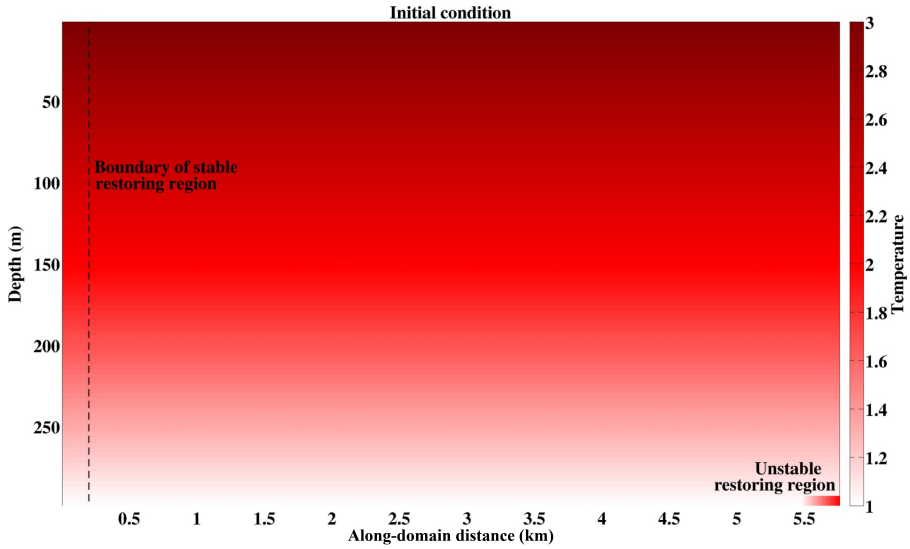


**Figure S5 | Initial condition in the Main simulation of an idealised meltwater outflow from beneath an Antarctic ice shelf.** The initial temperature distribution is shown by the colour shading, and the locations of the unstable restoring region (representing the meltwater outflow) and of the stable restoring region (representing ambient offshore conditions) are indicated.

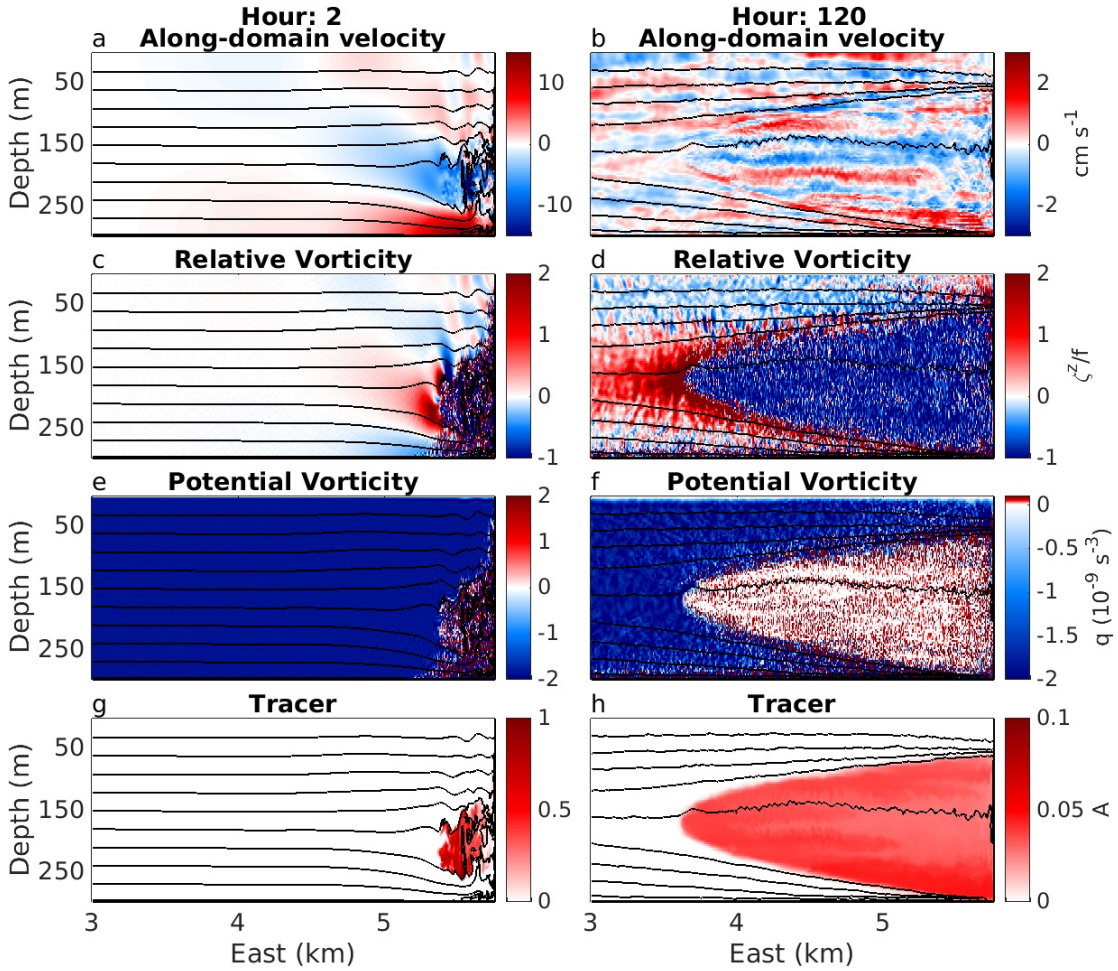


983

984 **Figure S6 | Evolution of the idealised meltwater outflow in the Main experiment.**

985 Distributions of the (a) along-domain velocity, (c) relative vorticity normalised by the

986 planetary vorticity, (e) potential vorticity and (g) passive tracer concentration, 2 hours

987 after the start of the simulation. Panels (b), (d), (f) and (h) show the same variables as

988 (a), (c), (e) and (g), respectively, 120 hours after the start of the simulation.

989 Temperature contours are shown at intervals of 0.2°C in all panels. Units are

990 indicated next to the colour bars.

991

992

993

994

995

996

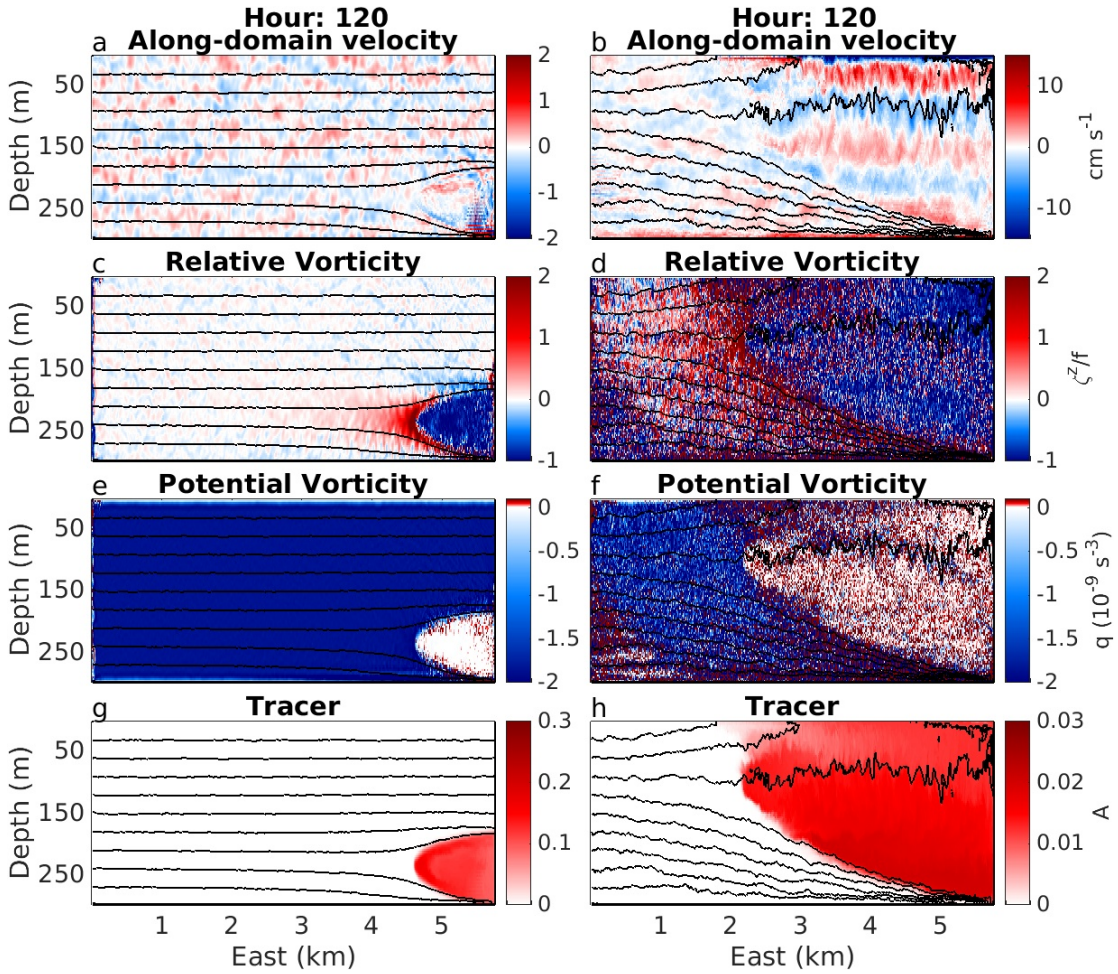


**Figure S7 | Evolution of the idealised meltwater outflow in the Perturbation experiments with reduced and enhanced forcings.** Distributions of the (a) along-domain velocity, (c) relative vorticity normalised by the planetary vorticity, (e) potential vorticity and (g) passive tracer concentration, 120 hours after the start of the reduced forcing (0.5 K) simulation. Panels (b), (d), (f) and (h) show the same variables as (a), (c), (e) and (g), respectively, 120 hours after the start of the enhanced forcing (1.5 K) simulation. Temperature contours are shown at intervals of 0.2°C in all panels. Units are indicated next to the colour bars.

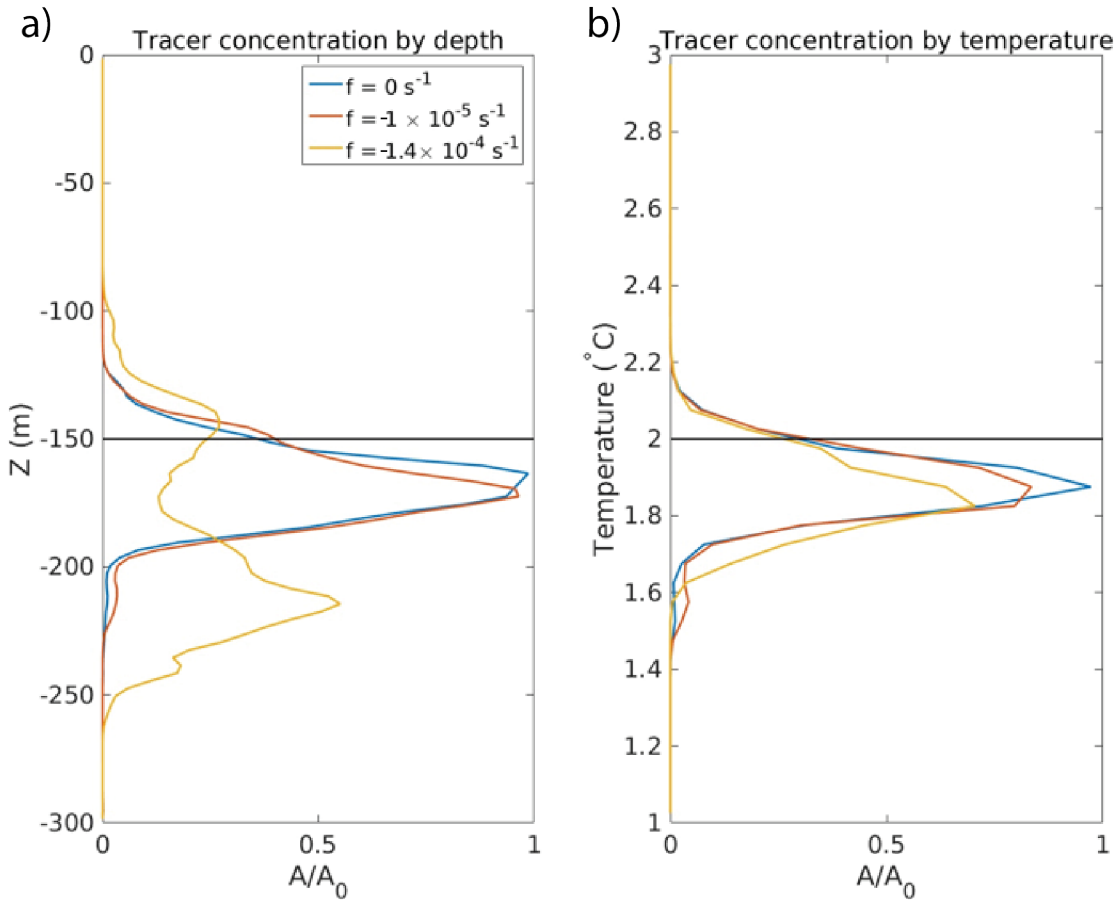


**Figure S8 | Vertical distribution of passive tracer on day 1 for varying planetary rotation.** (a) Horizontally integrated tracer concentration (normalised to a common value) as a function of depth for the Main experiment with realistic rotation ($f = 1.4 \times 10^{-4}$ s$^{-1}$), and for the two Rotation experiments with weak ($f = 1 \times 10^{-5}$ s$^{-1}$) and no ($f = 0$) rotation. (b) Domain-mean tracer concentration (normalised to a common value) in temperature bins of 0.05 K width. The (a) depth or (b) temperature of neutral buoyancy for the simulated outflow is shown as a horizontal black line.